Focussing frustration for self-limiting assembly of flexible, curved particles

Nabila Tanjeem,[1] Douglas M. Hall,[2] Montana B. Minnis,[1] Ryan C. Hayward,[1] and Gregory M. Grason[2]

[1] *Department of Chemical and Biological Engineering, University of Colorado, Boulder, Colorado 80303, USA*

[2] *Department of Polymer Science and Engineering, University of Massachusetts, Amherst, Massachusetts 01003, USA*

We show that geometric frustration in a broad class of deformable and naturally curved, shell-like colloidal particles gives rise to self-limiting assembly of finite-sized stacks that far exceed particle dimensions. When inter-particle adhesions favor conformal stacking, particle shape requires *curvature focussing* in the stack, leading to a super-extensive accumulation of bending costs that ultimately limit the ground-state stack size to a finite value. Using a combination of continuum theory and particle-based simulation, we demonstrate that the self-limiting size is controlled by the ratio of the intra-particle stiffness to inter-particle adhesion, ultimately achieving assembly sizes that are tuned from a few, up to several tens of, particles. The range of self-limiting assembly is delimited by the two structural modes of "frustration escape" which evade the thermodynamic costs of curvature focussing. Crucially, each of these modes can be suppressed through suitable choice of adhesive range and patchiness of adhesion, providing feasible strategies to program finite assembly size via the interplay between shape-frustration, binding and deformability of colloidal building blocks.

Advanced methods to control the size, shape and interactions of synthetic particles [1–4] continue to drive remarkable progress in formation of hierarchical structures via colloidal assembly. Yet, the prevailing paradigms almost exclusively target nearly strain-free structures, whose equilibrium dimensions grow to uncontrolled sizes to minimize free energy. In contrast, several recent studies and models point to the possibility of exploiting the size-dependent costs of geometric frustration to control the equilibrium finite size and shape of assemblies [5–14]. Biological systems taken advantage of functional properties of a diverse range of finite assemblies from viral capsids [15–17] and bacterial microcompartments [18, 19] to structurally colored protein superstructures [20–22] and multi-filament bundles [23, 24].

Self-limitation in frustrated systems occurs when misfits between the subunits shapes incur elastic costs for assembly that accumulate superextensively with assembly size [5]. When those costs balance cohesive interactions, they define a thermodynamically selected finite size that can, in principle, substantially exceed the sizes of subunits or their interaction range. Self-limitation implies a minimum in the assembly free energy per subunit at finite aggregation number as well as a *pseudo-critical aggregation transition* to a state dominated by finite aggregates at high enough subunit concentration [25]. Notably, self-limitation by frustration falls into a fundamentally distinct class from more familiar self-limiting equilibrium mechanisms, including finite-diameter protein tubules and shells [26] and micellar aggregates of amphiphiles [27]. In these examples, the curvature of subunits leads the assembly to close upon itself, achieving a finite size that determined by the degree of curvature per subunit. In frustrated assemblies, the ability of an aggregate to "sense" the distance between its open boundaries relies on formation of coherent *gradients* of inter-subunit stress [10].

To date, understanding of this paradigm derives almost exclusively from continuum theories, where the elastic costs and magnitudes of frustration are phenomenological parameters, and intra-assembly stresses are modeled in simplified morphologies [6, 7, 12, 28–31]. As such, these models fail to survey the low-energy, symmetry-breaking modes of "frustration escape" by which physical assemblies evade the costs of accumulating frustration. The few discrete -subunit models of frustrated assembly studied so far consider only minimal descriptions of elastic polygons with infinitely short-ranged binding interactions, and coarse-grained (i.e. vertex based) elasticity models [8, 10, 11]. Such models leave open key basic questions: what is the accessible range of self-limiting assembly for a given frustrated particle design? How are self-limitation, or frustration escape, controlled by shape, deformability and interactions of particles?

In this article, we demonstrate the design of frustrated colloidal particles that exhibit tunable self-limiting assembly sizes. The misfitting subunits are deformable, curved elastic shells (dubbed 'curvamers') that stack face-to-face due to short-ranged attractions. Uniform spacing between conformally-contacting curvamers, however, yields gradients of local curvature along the stacks (Fig. 1b), a phenomenon well known in focal conic domains of liquid crystals and geometric optics [32–35], but which here provides a mechanism to propagate frustration to especially large inter-particle scales. Analogous frustration is known in nematic-bend phases of repulsive "banana shaped" particles [36, 37], but it has only recently been recognized to give rise to accumulation elastic energy with domain size in their ground states [38, 39]. Here, we show by a combination of analytical theory and coarse-grained particle simulations that careful design of the ratio of elastic costs of particle bending and inter-particle adhesion leads to selected finite sizes up to at least several 10s of curvamers. We further establish that ground states escape frustration through principally two distinct mechanisms of "curvature defocussing", but that

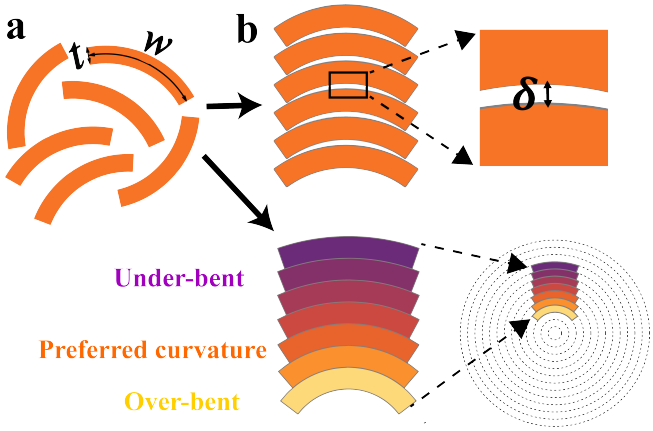

Figure 1. **(a)** Curvamers with preferred curvature radius r_0. **(b)** Top: Stacking of undeformed curvamers with a nominal separation distance δ. Bottom: Curvature-focussing, concentric stacking of flexible curvamers (i.e. conformal contact).

self-limitation can be maintained through suitable control of interaction range and patchiness, design principles that should be readily achievable with a range of synthetic colloidal building blocks.

I. CONTINUUM MODEL OF CONFORMAL STACKING

We begin by developing a simplified analytical theory of assembly of cylindrically curved shells, which we model in terms of their 2D cross-sections, ignoring distortions along their axial direction. As shown in Fig. 1a, the geometry of each curvamer is defined by a preferred curvature κ_0 (i.e. $r_0 = \kappa_0^{-1}$ is the radius of curvature of the midline), thickness t, and width w. If curvamers retain their preferred shape, non-overlap between shells requires a gap between curvamer surfaces, which is maximal at their centers $\delta \approx tw^2\kappa_0^2/8$. The condition of face-to-face assembly with a perfect, conformal contact requires the curvamers to bend and deviate from a fixed shape (Fig. 1b). To stack the $(n+1)$th curvamer on top of curvamer n, perfect contact requires a concentric stacking, or $r_{n+1} - r_n = t$, or

$$\kappa_{n+1} = \frac{\kappa_n}{1+\kappa_n t}. \tag{1}$$

This is the condition of *curvature focussing* required by constant spacing between curved surfaces, which introduces shape gradients at the expense of elastic costs of over- and under-bending of particles. The energy of a stack of N curvamers is the sum of the adhesive gain ($E_{\rm ad}$) and elastic bending costs ($E_{\rm el}$),

$$E(N) = E_{\rm ad}(N) + E_{\rm el}(N) = -\gamma A(N-1) + \frac{BA}{2}\sum_{n=1}^{N}(\kappa_n - \kappa_0)^2, \tag{2}$$

where γ and B are the adhesive energy (for perfect contact) per unit area and curvamer bending modulus, respectively, and A the area of curvamer surfaces. To understand the mechanism of self-limitation, we consider the limit of stacks that are short compared to r_0, which can be analyzed in terms of the curvature at a layer height z relative to a mid-layer of preferred shape, which according to eq. (1) exhibit a linear variation in bending $\kappa(z) \simeq \kappa_0 - \kappa_0^2 z$. Averaging bending cost over the stack of size N, we expect $E_{\rm el}(N) \approx BA\kappa_0^4 t^2 N^3/24$.

Assemblies are dominated by the aggregates that minimize the (intra-aggregate) interaction free energy per subunit [40]. Here, we focus on what limits the existence of minimum at finite size for sufficiently low T, and hence neglect corrections to the assembly energetics arising from intra-aggregate fluctuations, whose dominant entropy is expected to be extensive in aggregate size for large size. We discuss the role of entropic contributions in the self-limiting assembly of curvamers below. Considering the "short stack" energy per subunit

$$E(N)/(AN) \approx -\gamma + \gamma/N + B\kappa_0^4 t^2 N^2/24 \tag{3}$$

, we thus expect a selected size

$$N_{\rm min} \approx (12\gamma/B\kappa_0^2)^{1/3}(\kappa_0 t)^{-2/3}. \tag{4}$$

A more complete analysis of the continuum model (see Appendix A) shows that this power-law growth of the self-limiting stack persists up to a size $N_{\rm min} \lesssim r_0/t$ beyond which the selected sizes grow more rapidly as the mean curvature of all particles begins to flatten with stack growth. Defining the dimensionless adhesion-to-bending ratio $S \equiv \gamma t/B\kappa_0$, and scaled stack size $H = N\kappa_0 t$, the self-limiting size of conformal stacks satisfies the equation of state (Appendix Eq. A9)

$$S(H_{\rm min}) = \frac{2 - 2\sqrt{H_{\rm min}^2+1}}{H_{\rm min}} + \sinh^{-1} H_{\rm min} \tag{5}$$

According to this relationship, the power-law scaling for small stack size, $H_{\rm min}(S \ll 1) \sim S^{1/3}$, gives way to exponential growth $H_{\rm min}(S \gg 1) \sim e^S$ for large S.

II. SIMULATIONS OF DISCRETE CURVAMER STACKS

A. Finite size selection in colloidal model

Assuming perfect curvamer alignment and conformal contact, the continuum model predicts that the self-limiting stack size grows arbitrarily large with increasing S. To test the limits of self-limitation, specifically the ability of more complex relaxation modes of curvamer stacks to circumvent frustration, we turn to numerical simulations of a 2D coarse-grained curvamer model. We implement elastic shell mechanics via a bead-spring truss network (see Fig. 2a and Appendix B for more details),

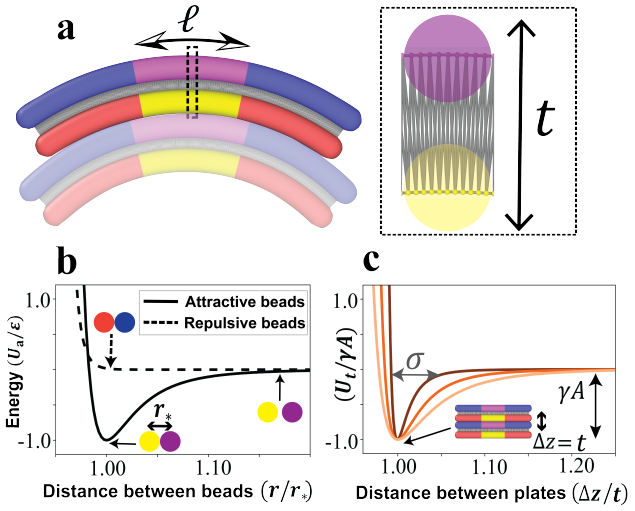

Figure 2. **(a)** Bead-spring construction of the curvamer model: interaction sites are labeled as colored beads connected by a truss network of harmonic springs (grey). **(b)** Pairwise potential between the red-blue pairs and the yellow-magenta pairs. Inter-curvamer attractions derive from attractive yellow-magenta LJ patches, with shorted-ranged repulsion in the red-blue flanks preventing overlap. **(c)** Total adhesion energy between two (flat) particles as function of scaled center-to-center spacing for variable attractive range $\sigma = 0.06t, 0.12t, 0.18t$.

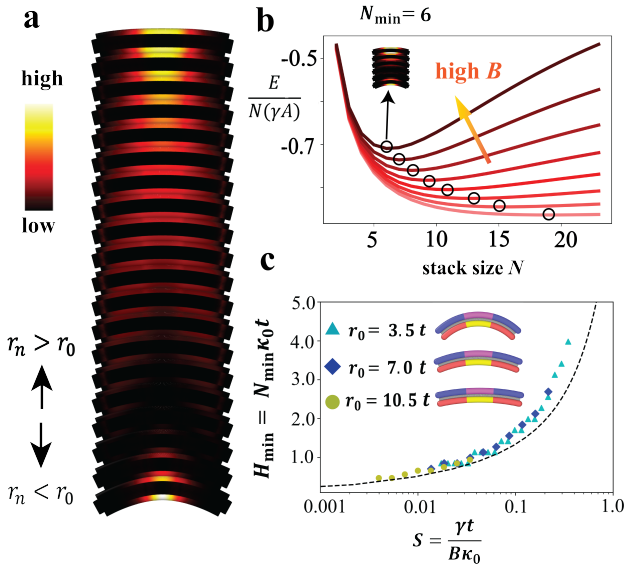

Figure 3. **(a)** Bond distortion for a stack with $N = 20$ at the ground state, with bright colors representing higher energy. Over/underbending deformations – stretching/compression of horizontal bonds on the top and bottom of particles – are prominent at the ends of the stack. **(b)** Normalized energy per curvamer as a function of stack size, where darker colors represent assemblies with higher bending modulus, where the ratios $\gamma/(B{\kappa_0}^2)$ and S were varied between $0.09 - 1.44$ and $0.01 - 0.22$, respectively (see design 2 on table S6). **(c)** Relationship between the dimensionless adhesion S and dimensionless stack size $H_{\min}$ for three different curvamer geometries with $\kappa_0 t = 0.29, 0.14, 0.09$. The dashed line shows the continuum model.

with rest lengths chosen to set the upper (+) and layer (-) curvature radii to $r_\pm = r_0 \pm \frac{t_0}{2}$ and $r_{\text{out}} = r_0 + \frac{t_0}{2}$, respectively. The isosceles trapezoidal unit cell of this bilayer structure (Fig. 2a) comprises horizontal, vertical and diagonal springs with stiffnesses set to achieve the bending mechanics of an elastic shell of thickness t_0 and Poisson ratio 0.3 (Fig. S3).

To model attractive interactions between curvamers, we parameterize pair-wise interactions between vertices on the inner and outer faces of two types: finite range attraction for an inner patch of width $\ell \leq w$ (magenta and yellow beads in Fig. 2a) and pure repulsion in the outer flanks of the particle (blue and red beads in Fig. 2a). The pairwise attraction between beads in the inner patch is given by a shifted Lennard-Jones (LJ) potential

$$U_a(r) = 4\epsilon \left[\left(\frac{\sigma}{r - \Delta} \right)^{12} - \left(\frac{\sigma}{r - \Delta} \right)^{6} \right], \qquad (6)$$

where σ is the range of the attractive well and Δ is a shift parameter that controls the equilibrium separation $r_* = 0.71 t_0$ between attractive sites independent of σ. The LJ potential (with beads placed at a high linear density, $\lambda = 16.1 t_0^{-1}$) is designed to model favorable uniform and frictionless contact with center-to-center spacing between bound curvamers $t = t_0 + r_*$. Outside of this attractive zone, repulsive interactions (with beads at the same density λ) are modeled by a Weeks-Chandler-Anderson like potential whose smooth cut-off is matched to the minimum of $U_a(r)$ at r_*, such that at perfect conformal contact, repulsive sites do not contribute to the net interaction energy between bound curvamers (the repulsion strength is set to $10^{-3}\epsilon$, with ϵ the attractive strength in Eq. 6). We define $-\gamma A$ as the total attractive potential between two conformally contacting curvamers, and compute it as the depth of attractive interactions for two planar particles (i.e. flattened shells) shown in Fig. 2c. We expect a dependence of $\gamma \propto \epsilon \ell \sqrt{r_* \sigma} \lambda^2$ and a surface-surface interaction range is close to σ (Fig. 2c). To map coarse-grained curvamer parameters to the dimensionless adhesion S, we assume γ to be independent of particle curvature, and further measure the shell stiffness B by computing curvamer energy for variable circular curvatures of the midline (see Figs. S2 and S3).

To assess the assembly energy landscape via a particle-based model of curvamers, we perform energy minimization for stacks of N curvamers, analyzing first the case of $\ell = w/3$, $\sigma = 0.06t$ and $r_0 = 7.0t$. Beginning from a (curvature focussing) configuration of concentrically stacked particles, energy is relaxed via a conjugate gradient algorithm in LAMMPS [41]. We verify in Appendix I that minimization from this initial configuration generically achieves the lowest energy per particle compared to distinct initial configurations states. The thermal stability

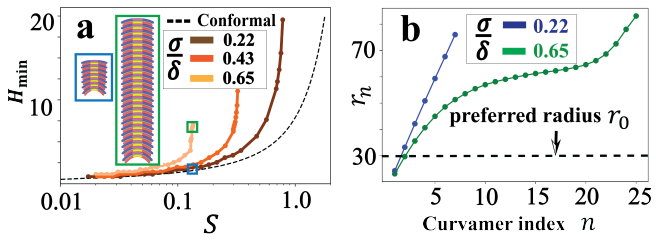

Figure 4. **(a)** Self-limiting stack size vs. dimensionless adhesion for three different ratios of attraction range (σ) to nominal gap size (δ). The two stacks on the inset represent the self-limiting stacks for $\frac{\sigma}{\delta} = 0.22$ and $\frac{\sigma}{\delta} = 0.65$ at the same dimensionless adhesion indicated by the small blue and green squares, respectively.**(b)** The radii of curvature (r_n) of each curvamer in the two stacks plotted against their position index n. The dashed line shows the preferred radius r_0.

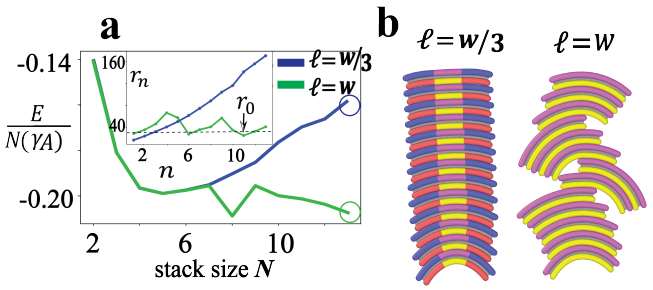

Figure 5. **(a)** The energy density for two different adhesive path sizes for $\sigma = 0.06t$, $r_0 = 3.5t$ and $S = 0.07$. For $\ell = w/3$ (blue) a minimum indicates a self-limited stack size $N_{\min} = 5$, while for $\ell = w$ (green) energy density decreases below a metastable minimum at large N. Curvature radii in the corresponding $N = 13$ stacks are plotted in the inset. **(b)** Comparison on $N = 13$ stack configurations for $l = w/3$ and $\ell = w$.

of these ground states was studied via simulated annealing as described in Appendix F. Fig. 3a shows the energy density in the horizontal springs due to variable curvature through the stack thickness (Fig.S8) for the ground state of an $N = 20$ curvamer stack. The energy per curvamer plotted in Fig. 3b as a function of the stack size for a sequence of increasing bending stiffness (corresponding to $S = 0.01 - 0.22$) shows a global minimum at $N_{\min}$, indicative of self-limiting stack assembly [42]. Notably, the energy minimum shifts to smaller $N_{\min}$ with increased bending stiffness (Fig. 3b).

These results confirm that the self-limitation derives from the accumulated bending strain generated via curvature-focussing stacking geometry, and further that the equilibrium stack size *decreases* with that elastic cost. In Fig. 3c we compare the optimal stack sizes from the discrete curvamer model to the continuum results in eq. (5) for uniform conformal contact. Considering more than two orders of magnitude in dimensionless adhesion to bending stiffness ratios S, we find that results from three different particle curvatures collapse onto a single curve whose monotonic increase with S shows good agreement with the conformal contact model, notwithstanding the fact that equilibrium shapes of discrete curvamers (Fig. 3a) deviate considerably from the idealized circular shapes assumed in the model. In the cases summarized in Fig. 3, self-limitation relies on the propagation of curvature focussing from one end of the stack to the other, leading to self-limiting sizes that far exceed the single building block size (i.e. $N_{\min} \gg 1$). Next, we investigate two mechanisms through which assemblies can "defocus" curvature propagation and escape the cumulative costs of frustration.

B. Mechanisms of frustration escape and limits of finite-size selection

The first mode of escape is observed when adhesive interactions between curvamers are sufficiently long-ranged. Intuitively, this can arise when σ is much larger than the nominal gap size δ between undeformed curvamers, in which case the pair maintains strong adhesion without shape change, or its elastic cost. Fig. 4 shows results for optimal stack sizes for curvamers of constant shape ($r_0 = 3.5t$), but varying ratio of adhesive range to nominal gap size, σ/δ. The equilibrium stack size generally exceeds the values predicted for perfect conformal contact, but also increases with the interaction range for a fixed dimensions adhesion S. For example, for $S = 0.14$, the optimal stack grows from $N_{\min} = 7$ for $\sigma/\delta = 0.22$ to $N_{\min} = 25$ for $\sigma/\delta = 0.65$ (Fig. 4a). Further, in clear distinction to the conformal contact model, which predicts self-limiting stacks for all S, we observe an upper limit to the adhesion strength $S_{\max}$ above which no minimum in $E(N)/N$ can be identified, which decreases with increasing σ (Fig. 4a and Fig. S10). To explain these effects, we compare the shape profiles of optimal curvamer stacks with two values of interaction range, $\sigma/\delta = 0.22$ and 0.65 in Fig. 4b. While shorter range interactions (blue curve) yield curvature radii that increase roughly linearly with n, corresponding to curvature-focussing, longer range interactions (green curve) provide a slower and non-linear increase of curvature radius along the stack. This nonlinear profile indicates the opening of a small gap between curvamer faces (see Fig. 14), allowing interior curvamers to maintain relaxed and roughly constant curvature shapes closer to the preferred shape. Hence, the longer range interactions shift the effect of frustration to strain inter-particle bonds, weakening the effect of curvature frustration. Thus, as σ increases for a fixed S, the cumulative elastic costs of frustration are reduced, allowing optimal stacks to reach larger sizes. Ultimately, the assembly "escapes" frustration when the accumulating elastic costs of curvature focussing overwhelm the cost of uniform shape, gap-strained stacking.

The second mode of escape develops by "misalignment"

of curvamer binding, and is observed when the size of binding patch ℓ is increased, permitting low-cost lateral sliding of bound curvamers. In Figure 5 we compare assembly for short-range adhesion ($\sigma/\delta = 0.22$) for particles with a narrow ($\ell = w/3$) and broad ($\ell = w$) adhesive binding patch. In particular, we consider the energetic ground states resolved when subjecting the initially aligned assemblies to simulated annealing at finite temperature (see Appendix F). Notably, the curvamer stacks with narrow binding patches retain their alignment, such that curvature focussing propagates throughout the stack height. In comparison, assemblies of curvamers with broad binding patches become unstable to lateral rearrangement between adjacent curvamers in the stack. This results in large complex "super -stacks" composed of looser assembly of multiple aligned and concentric "substacks" of $\sim 2-4$ units. The lateral sliding between adjacent sub-stacks effectively redirects the curvature focussing to outside of the assembly, allowing the super-stack to grow larger without generating superextensive elastic costs for shape change.

III. DISCUSSION AND CONCLUDING REMARKS

In summary, we have demonstrated that geometry of curvature focussing can be used to design frustration-limited assemblies of curved colloidal particles, and crucially, explored how particle-scale features controlling interactions inhibit or allow the assembly to escape the thermodynamic consequences of geometric frustration. Taken together, these results point to critical features required for achieving large self-limiting dimensions for frustration-limited assemblies of curved colloidal particles: (i) inter-particle adhesion that is effectively "stiffer" than required intra-particle deformation and (ii) interactions that maintain alignment of curvature frustration throughout the assembly. Given that these criteria are met, self-limitation of curvamer assemblies offers important advantages over other mechanism of engineered frustration, specifically, the especially large range of self-limiting stack sizes relative to the single particle size. For example, a recent experimental design of incommensurate DNA origami particles reports self-limiting chains of mean length ≤ 5 particles or less [9], while simulations of frustrated tubules reported free energy minima only up to $\sim 4-8$ particle lengths [11]. As the "escape size" of assembly derives from the generic competition between elastic costs of accumulating frustration versus "flattening out" misfit in an infinite assembly [25]. In curvamer assembly, the latter cost exceeds the former until the stack thickness reaches $\sim r_0$, which can be made arbitrarily large simply by decreasing precurvature, accounting for the large range of equilibria ($N_{\min} \sim 3-70$) exhibited in our model.

We note that this large range of self-limiting sizes is expected to be experimentally accessible with synthetic, shape-controlled colloidal systems. Curved shell-like colloidal particles meeting the design specifications illuminated here can be synthesized using shape-shifting hydrogel [43] or geometrically-programmed DNA origami particles [44, 45]. Recently, photolithography of bilayer hydrogel films has been used to fabricate curved particles on the colloidal scale [46]. Potential routes to drive curvamer assembly include short-ranged depletion [6, 47] or DNA-hybridization interactions [48], both of which can be engineered to maintain a patchy character. Considering an adhesive attraction of $\gamma A \approx 10\, k_B T$ between shell-like colloids with $w \sim 5\ \mu$m and $t \sim 50$ nm for elastomeric curved shells with pre-curvatures $\kappa_0 t \sim 10^{-3} - 10^{-1}$ we expect a bending stiffness in the range $B \sim 10^3 k_B T$ [49], for which our model predicts self-limitation up to $N_{\min} \sim 10^2$. This especially large size range depends on the unique mechanism of elastic energy accumulation in curvature focussing assembly, and therefore exhibits a strong dependence precurvature, $N_{\text{sim}} \sim \kappa_0^{-4/3}$, which grows especially large as curvature is tuned down.

We conclude with a brief discussion of the role of entropy in the self-limiting assembly of curvamers. The primary entropic costs of assembly arise from the translation entropy a free subunit gives up to join a large aggregate. For self-limiting assemblies [25, 27], this entropic trade-off sets a concentration and temperature dependent criterion for assembly, quantified by the so-called *critical aggregation concentration*, $\phi_* \simeq e^{\epsilon_*/k_B T}$, where ϵ_* is the minimum of the aggregation free energy per subunit $\epsilon(N = N_{\min})$. Above saturation, i.e. when $\phi \gg \phi_*$, the energetic benefits to assemble into aggregates of size $N_{\min} \gg 1$ overwhelm the translational entropy loss of free subunits, and all but a neglible fraction of the total subunit mass is distributed in aggregates peaked around $N = N_{\min}$ (and with a size dispersity inversely proportional to $\sqrt{N_{\min}\epsilon''(N_{\min})/k_B T}$). To a first approximation, at sufficiently low-temperatures $\epsilon_* \simeq E(N_{\min})/N_{\min}$, which is directly given by the energetic balance between adhesion and elastic energy accumulation in curvature stacks described above.

Non-zero temperature will lead to aggregation free energy corrections for a stack of size N of the form $\Delta F(N) \approx k_B T\big[N\delta\epsilon_0 + \delta\epsilon_{\text{sub}}\big]$. Here, $\delta\epsilon_0$ represents the leading contributions arising from both the orientational entropy difference between free and assembled curvamers as well as the leading terms in the vibrational entropy of the aggregate (i.e. akin to a fluctuating 1D chain), both of which are expected be of order unity. Note this leading term does not alter the N-dependence of $\epsilon(N)$ (or the size of optimal stack), but only shifts the N-independent value of ϵ_*, and hence the temperature and concentration dependent threshold for aggregation ϕ_*. The subleading terms $\delta\epsilon_{\text{sub}}$ are $\mathcal{O}(N^0)$ (or logarithmic) and hence primarily alter the N dependence of $\epsilon(N)$ through a shift of the magnitude of the $1/N$ terms, in other words, a temperature dependent correction to the γ/N surface contributions. As the selected size (deep in the self-limiting regime) scales weakly with the sur-

face term, i.e. $N_{\min} \sim \gamma^{1/3}$, a downward shift in the effective value of γ by a few k_BT will not alter the order of magnitude optimal size, which is most strongly sensitive to the controlled *precurvature* of particles. The expected insensitivity of size limitation to entropic corrections to the aggregation free energy in the curvamer model is consistent with recent non-zero-T simulations of a distinct discrete-unit model of frustrated assembly, non-Euclidean tubules [11].

ACKNOWLEDGMENTS

We are grateful to K. Sullivan and C. Santangelo for extensive discussions on this work. This work was supported by the Brandeis Center for Bioinspired Soft Materials, an NSF MRSEC, DMR-2011846 (NT, DMH, MBM RCH, GMG), and through NSF grant No. DMR-2028885 (DMH, GMG).

Appendix A: Continuum model of aligned, conformally-stacked curvamer energetics

Here, we describe the energetics of aligned, conformally-stacked curvamers. Specifically, we consider stacks of N particles, each of which is assumed to obey the condition for perfect, conformal contact,

$$\kappa_{n+1} = \frac{\kappa_n}{1+\kappa_n t}, \tag{A1}$$

where κ_n is the curvature of the nth particle in the stack, and the $(n+1)$th particle is attached to the convex face of the nth particle. Here we assume that curvature is *uniform* along the curvamer so that the condition of eq. (A1) implies that curvamers are concentrically stacked circular arcs throughout the stack, such that the curvature of all particles can be parameterized by the curvature κ_- of a fictitious $n = 0$ particle at the bottom of the stack,

$$\kappa_n = \frac{\kappa_-}{1+\kappa_- nt}. \tag{A2}$$

From this the total elastic energy of the stack is simply,

$$E_{\rm el}(N,\kappa_-) = \frac{BA}{2}\sum_{n=1}^{N}\left(\kappa_n-\kappa_0\right)^2 \simeq \frac{BA}{2}\int_0^N dn\,\left(\kappa_n-\kappa_0\right)^2. \tag{A3}$$

where in the limit of $N \gg 1$ the discrete sum is well-approximated by the integral given on the right-hand side. To evaluate this, it is most convenient to define the reduced curvature $k \equiv \kappa_-/\kappa_0$ and the scaled height in the stack $h \equiv n\kappa_0 t$, such that the elastic energy takes the form,

$$\begin{aligned} E_{\rm el}(H,k) &= \frac{BA\kappa_0}{2t}\int_0^H dh\,\left(\frac{k}{1+kh}-1\right)^2 \qquad (A4)\\ &= \frac{BA\kappa_0}{2t}\Big[\frac{H+kH(H+k)}{1+kH} - 2\ln\left(1+kH\right)\Big], \end{aligned}$$

where $H = N\kappa_0 t$ is the reduced stack size. For a given stack size the curvatures adjust to minimize the elastic energy, with an equilibrium determined by $\partial E_{\rm el}/\partial k = 0$, which has the solution $k_*(H)$,

$$k_*(H) = 1 - H^{-1} + \sqrt{H^{-2}+1}. \tag{A5}$$

At the bottom of the stack the curvature varies from the preferred precurvature for short stacks (i.e. $k_*(H \to 0) \to 1$) to a maximal overcurvature at large stack sizes (i.e. $k_*(H \to \infty) \to 2$).

Inserting the size-dependent curvature into eq. (A4) yields the variation of elastic energy on stack size,

$$E_{\rm el}(H,k_*(H)) = \frac{BA\kappa_0}{2t}\Big[\frac{2\sqrt{H^2+1}-2+H^2}{H} - 2\sinh^{-1}H\Big]. \tag{A6}$$

Notably, this elastic energy exhibits superextensive growth for small stack sizes $E_{\rm el} \sim H^3$. This derives from the fact that for short stacks, bending strain varies linearly in the stack about a "neutral" central particle. For large stacks, constituent particles flatten with increased size, leading to an asymptotically constant elastic cost per particle $E_{\rm el} \sim H$.

Combining the size-dependent elastic energy with cohesive energy between the curvamers, we have the total stack energy,

$$E(N) = -\gamma A(N-1) + E_{\rm el}(N), \tag{A7}$$

where γ is the cohesive energy per unit length of curvature contact. To assess the size selectivity of the competition between cohesion and elasticity, we consider the scaled energy per particle,

$$\frac{E(H)}{N} = BA\kappa_0^2\left(\frac{S}{H} + \frac{1}{2}\Big[\frac{2\sqrt{H^2+1}-2+H^2}{H^2} - \frac{2}{H}\sinh^{-1}H\Big]\right) - \gamma A, \tag{A8}$$

where $S \equiv \frac{\gamma t}{B\kappa_0}$ is the reduced adhesion. For a given S the equilibrium stack size is determined by the minimum of eq. (A8) with respect to H, yielding an equation of state relating optimal stack size H_* to cohesion,

$$S(H_{\min}) = \frac{2-2\sqrt{H_{\min}^2+1}}{H_{\min}} + \sinh^{-1}H_{\min} \tag{A9}$$

This relationship exhibits a power law relationship at small size, $S \sim H_*^3$, corresponding to $H_{\min} \sim S^{1/3}$. Whereas in the large stack limit, $S \sim \ln 2H_{\min}$, corresponding to an exponential growth of stack size with cohesion $H_{\min} \sim e^S$

Appendix B: Design of a curvamer

The geometry of a curvamer is determined from three independent parameters, r_0, θ_0, and t_0 as shown in table

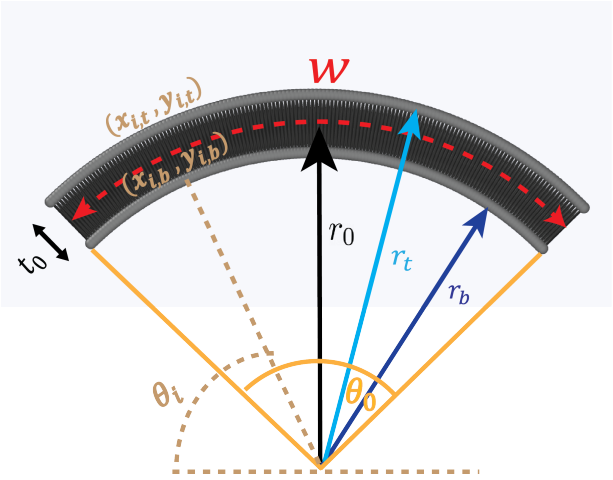

Figure 6. Design of a curvamer particle.

Table I. Radius, thickness, and width of curvamers

Parameter	Design 1	Design 2	Design 3
r_0	30	60	90
θ_0 (°)	90	45	30
t_0	5.0	5.0	5.0
$w = r_0\theta_0$	47.124	47.124	47.124

I. Design 1, design 2, and design 3 represent the curvamers on Fig. 3c of the main manuscript. The internal network of elastic springs is a repeating array of trapezoidal trusses, of vertical height t_0 and respective upper (top) and lower (bottom) horizontal edge widths d_t and d_b .

To calculate the Cartesian coordinates of the beads in the curvamer, their corresponding polar angles θ_i were calculated from the total angular envelope θ_0. From the minimum angle $\theta_{\min} = 90 - \frac{\theta_0}{2}$ and the maximum angle $\theta_{\max} = 90 + \frac{\theta_0}{2}$, we find $\theta_i = \theta_{\min} + i\frac{\theta_{\max}-\theta_{\min}}{n-1}$, where $n = 150$. The radius of curvature of the first bead layer, $r_b = r_0 - \frac{t_0}{2}$ and the radius of curvature of the second bead layer, $r_t = r_0 + \frac{t_0}{2}$. From these values, the positions of all beads on both of the layers are calculated as described below.

Beads on the first layer:

$$x_{i,b} = A + r_b\cos(\theta_i), \tag{B1}$$

$$y_{i,b} = B - \frac{t_0}{2} - r_b(1 - \sin(\theta_i)) \tag{B2}$$

Beads on the second layer:

$$x_{i,t} = A + r_t\cos(\theta_i) \tag{B3}$$

$$y_{i,t} = B + \frac{t_0}{2} - r_t(1 - \sin(\theta_i)), \tag{B4}$$

where (A, B) is the center of the curvamer.

The spring constants are chosen to match the elastic response of a thin isotropic plate of thickness t_0, Young's modulus E and Poisson's ratio ν, derived for the flat case $\kappa_0 = 0$. The moduli of such a plate associated with uniform bending, stretching and shear deformations are $B = Et_0^3/(12(1-\nu^2)), Y = Et_0/(1-\nu^2)$ and $S = Et_0/(2(1+\nu))$, respectively. The deformations are related to the spring deformations of each trapepezoidal unit cell within the particle (considering the symmetric case $d = d_b = d_t$): bending strain κ results in elastic energy per unit cell

$$E_{bend} = \frac{1}{4}d^2h^2k_h\kappa^2, \tag{B5}$$

for transverse stretching ratio ϵ

$$E_{stretch} = \frac{d^4(k_c + k_h) + d^2h^2k_h(2k_c + k_v)}{d^2k_v + h^2(2k_c + k_v)}\epsilon^2 \tag{B6}$$

and shear σ,

$$E_{shear} = \frac{d^2h^2}{d^2 + h^2}k_c\sigma^2. \tag{B7}$$

From these three relations, conditions on the ratio of spring constants are

$$\frac{k_v}{k_h} = \frac{12t_0^2(1-\nu)}{4t_0^2 - 3d^2(1-\nu)} \tag{B8}$$

and

$$\frac{k_c}{k_h} = \frac{3(t_0^2 + d^2)(1-\nu)}{2t_0^2}, \tag{B9}$$

where d is the average distance between the beads and ν is the Poisson's ratio of the curvamer. Since the distance between the beads of the top (d_t) layer and the bottom layer (d_b) are different in the isosceles trapezoid, when $\kappa_0 > 0$ as shown in Fig. 2a, we consider the mean distance, $d_{\text{avg}} = d = \frac{d_b+d_t}{2}$, calculated from the bead positions. We keep the ratios $\frac{k_v}{k_h}$ and $\frac{k_c}{k_h}$ constant for all curvamer designs and bending moduli.

Appendix C: Measuring bending energy in curvamer model

To prepare a curvamer with a radius of curvature r' that is different from its preferred radius r_0, we calculate its new angular envelope $\theta' = \frac{w}{r'}$. Then we find the coordinates of the beads following the equations S11-S14. When the curvamer relaxes from a flat state to a curved state with preferred r_0, the first (bottom) layer of the beads shrinks and the second (top) layer of the beads

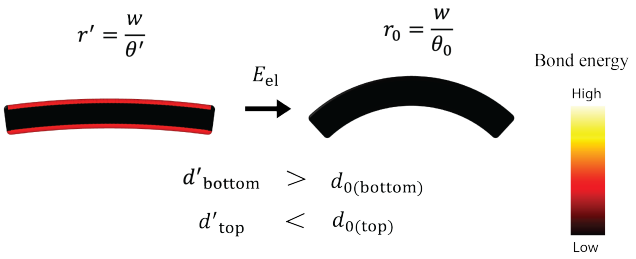

Figure 7. Bond energy mapping of a flattened curvamer that relaxes to its ground state. The higher bond energy at the initial state is shown by the red color. The bottom layer of the beads is stretched and the top layer of the beads is compressed in this state.

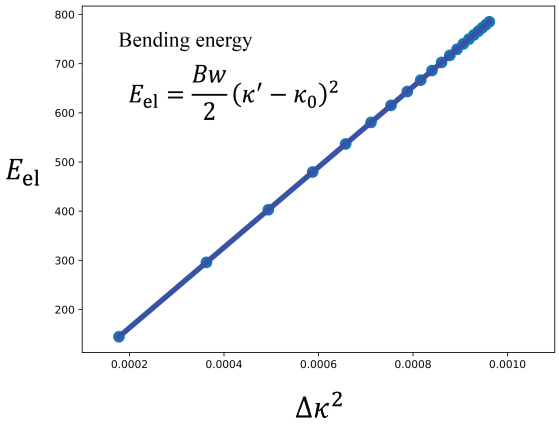

Figure 8. Linear elastic bending of a model curvamer demonstrated by the bending energy plot achieved from bending simulations.

Table II. Bead spacing, Poisson's ratio, and spring constant ratio

Parameter	Value
d	0.3163
ν	0.3
$\frac{k_v}{k_h}$	2.1044
$\frac{k_c}{k_h}$	1.0542

expands. We measure the bending energy in the simulation by relaxing a curvamer from different flattened states (different r' values) and confirm its linear relationship with increasing $(\Delta\kappa)^2$, (where $\Delta\kappa = \frac{1}{r_0} - \frac{1}{r'}$), that resembles a linear elastic material.

Appendix D: Adhesion between two flat plates

The total interaction potential between two flat plates are calculated by taking the sum of all the inter-bead potentials.

$$\gamma A = \sum_{i=1}^{n}\sum_{j=1}^{n} 4\epsilon \left[\left(\frac{\sigma}{r_{ij} - \Delta} \right)^{12} - \left(\frac{\sigma}{r_{ij} - \Delta} \right)^{6} \right] \quad \text{(D1)}$$

The yellow-magenta pairs contribute to the total plate potential significantly as their interaction strength ϵ is much larger than the interaction strength between red-blue pairs $\epsilon' < 0.0001\epsilon$ where ϵ' is the repulsive interaction coefficient.

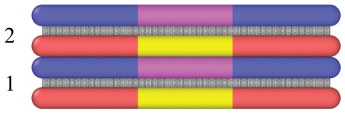

Figure 9. Adhesion energy γA is calculated by integrating the LJ-potential between the beads at top layer of plate 1 and the bottom layer of plate 2.

a. Choice of potential parameters To keep the equilibrium separation distance ($t = t_0 + r_* = 1.71t_0$) and the total adhesion energy (γA) between the plates constant for all different potential ranges σ, as shown in Fig. 2c in the main text, we adjusted the Δ and the ϵ parameters of the inter-bead potentials to maintain constant t and γA.

The values of the inter-bead LJ-potental parameters used in the simulations are listed in tables III, IV and V.

Table III. Short-ranged interaction $\sigma_1 = 0.06t$

Potential type	Parameter	Value
Attractive	σ_1	0.5
	Δ_1	3.02
	ϵ_1	3.0
Repulsive	σ'_1	0.5
	Δ'_1	3.2
	ϵ'_1	0.0001

Table IV. Medium-ranged interaction $\sigma_2 = 0.12t$

Potential type	Parameter	Value
Attractive	σ_2	1.0
	Δ_2	2.5
	ϵ_2	2.1
Repulsive	σ_2'	1.0
	Δ_2'	2.7
	ϵ_2'	0.0001

Table V. Long-ranged interaction $\sigma_3 = 0.18t$

Potential type	Parameter	Value
Attractive	σ_3	1.5
	Δ_3	2.0
	ϵ_3	1.7
Repulsive	σ_3'	1.5
	Δ_3'	2.1
	ϵ_3'	0.0001

Table VI. Simulation parameters used in Fig. 3c

Parameter	Design 1	Design 2	Design 3
r_0	30(3.5t)	60(7.0t)	90(10.5t)
σ	0.06t	0.06t	0.06t
k_h	$2.00 \times 10^3 - 3.98 \times 10^4$	$6.31 \times 10^3 - 1.0 \times 10^5$	$2.00 \times 10^4 - 3.16 \times 10^5$
BA	$7.42 \times 10^5 - 1.48 \times 10^7$	$2.34 \times 10^6 - 3.73 \times 10^7$	$7.42 \times 10^6 - 1.18 \times 10^8$
γA	1.00×10^3	9.97×10^2	3.31×10^2
$\frac{\gamma}{B}$	$1.00 \times 10^{-3} - 6.8 \times 10^{-5}$	$4.00 \times 10^{-4} - 2.68 \times 10^{-5}$	$4.46 \times 10^{-5} - 2.81 \times 10^{-6}$
S	$0.34 - 0.02$	$0.22 - 0.01$	$0.03 - 0.002$
$N_{\min}$	$14 - 3$	$19 - 5$	$10 - 5$
H	$3.96 - 0.85$	$2.69 - 0.71$	$0.94 - 0.47$

Table VII. Simulation parameters used in Fig. 4b

Parameter	Range 1	Range 2	Range 3
r_0	30(3.5t)	30(3.5t)	30(3.5t)
σ	0.06t	0.12t	0.18t
k_h	$8.81 \times 10^2 - 3.98 \times 10^4$	$2.15 \times 10^3 - 3.98 \times 10^4$	$5.29 \times 10^3 - 3.98 \times 10^4$
BA	$3.27 \times 10^5 - 1.48 \times 10^7$	$7.98 \times 10^5 - 1.48 \times 10^7$	$1.97 \times 10^6 - 1.48 \times 10^7$
γA	1.00×10^3	1.00×10^3	1.00×10^3
$\frac{\gamma}{B}$	$3.00 \times 10^{-3} - 6.83 \times 10^{-5}$	$1.3 \times 10^{-3} - 6.83 \times 10^{-5}$	$5.1 \times 10^{-4} - 6.83 \times 10^{-5}$
S	$0.78 - 0.02$	$0.32 - 0.02$	$0.14 - 0.02$
$N_{\min}$	$69 - 3$	$39 - 3$	$25 - 4$
H	$19.55 - 0.85$	$11.05 - 0.85$	$7.08 - 1.13$

Appendix F: Energy minimization methods

The initial state of a curvamer stack is prepared so that the first curvamer at the bottom of the stack is in its preferred radius r_0 and the subsequent curvamers have

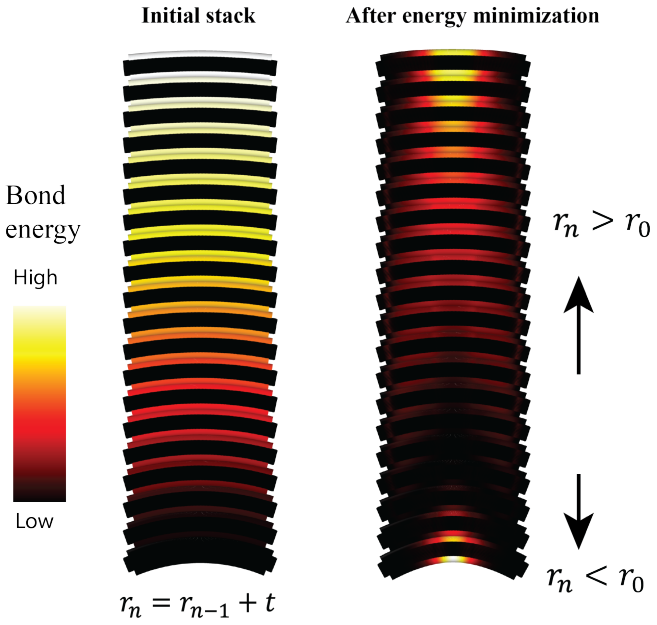

Figure 10. The initial (left) and the minimum-energy final (right) state of a curvamer stack.

increasing radii of curvature $r_n = r_{n-1} + t$, as shown in Fig. 10.

a. Conjugate gradient algorithm Energy minimization was implemented by using the built-in Polak-Ribiere version of the conjugate gradient (CG) algorithm in LAMMPS (https://docs.lammps.org/minimize.html). The stopping tolerance for energy, stopping tolerance for force, maximum iterations of minimizer, and maximum number of force/energy evaluations were set to 10^{-12}, 10^{-12}, 10^5, and 5×10^4.

b. Simulated Annealing We utilize Langevin dynamics to control the system's temperature over the course of the simulation https://docs.lammps.org/fix_langevin.html. The curvamers were cooled from $T_i = 1.2\epsilon/k_B$ to $T_f = 0.0001\epsilon/k_B$ over a period of 10^6 iterations, where each iteration represents a time step of $\tau = 0.001s$. During each time step, the mean squared displacement of each particle is $|\Delta \mathbf{r}|^2 = 4D\tau = 4\frac{k_B T}{\gamma_{drag}}\tau = 0.5 \times 10^{-4} t^2 (k_B T)$.

Appendix G: Radius of curvamers in a stack

We measure the radius of curvature of each curvamer in a stack r_n from the positions of the bead pairs. First, we find the midpoints of the line segments that connect the beads of the top layer $(P_1, Q_1, R_1, ...)$ to the beads of the bottom layer $(P_2, Q_2, R_2, ...)$. From the coordinates of every three midpoints (as shown by P, Q, R on the left panel of Fig. 12), we calculate a local radius of curvature. Finally, we calculate the average of all local radii measured from the triplets of adjacent points

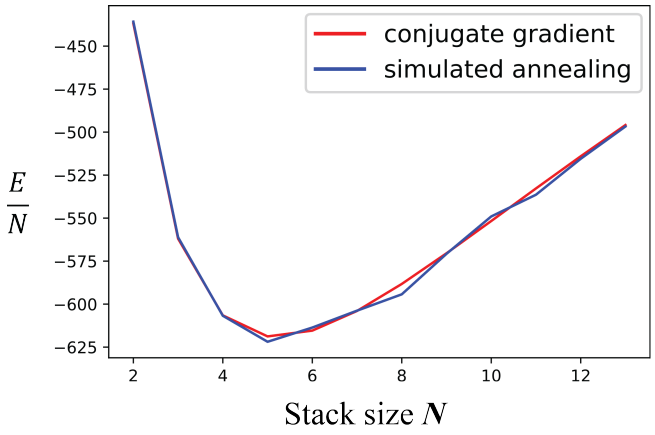

Figure 11. Energy density plot calculated using conjugate gradient algorithm and simulated annealing method show good agreement, both resulted in the energy minimum at $N = 5$.

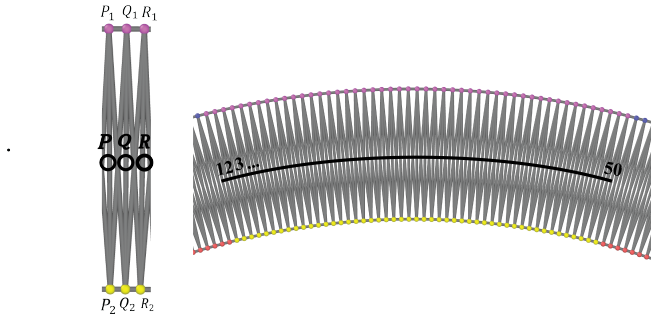

Figure 12. Left panel: the midpoints (P,Q,R) of the line segments connecting the beads on the two layers of a model curvamer. Right panel: All the midpoints in the patchy region of the curvamer, from which the average radius of curvature r_n is calculated.

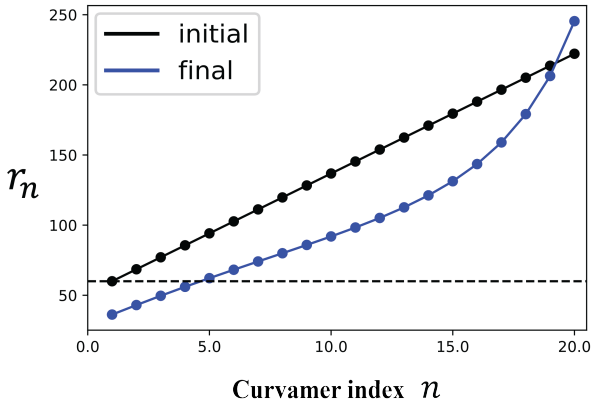

Figure 13. The radii of curvature of each curvamer in a stack of $N = 20$ as a function of their position index. The black plot shows the curvature at the initial state and the blue plot shows the curvature calculated at the ground state after energy minimization. The horizontal dashed line shows the preferred radius of curvature, $r_0 = 60$.

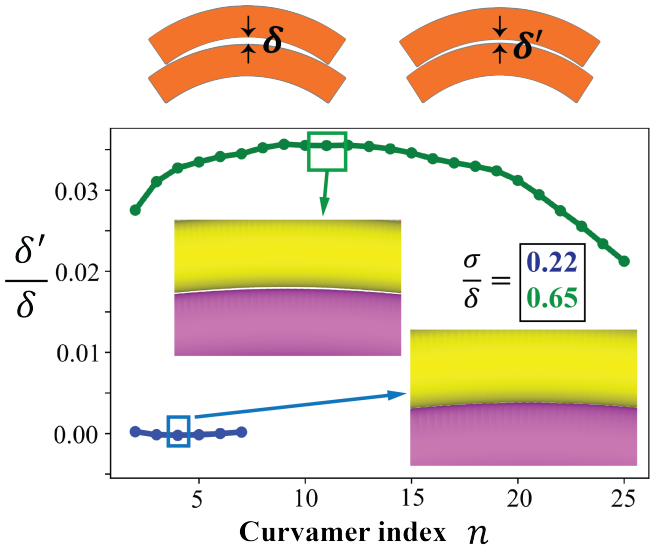

Figure 14. Gaps between n-th and $n+1$-th curvamer in the two stacks plotted as a function of curvamer position index. The magnified image of the gap between the 10th and 11th curvamer in the large stack ($\sigma/\delta = 0.65$) shows a small gap opening compared to the conformal contact between the 3rd and 4th curvamer in the small stack ($\sigma/\delta = 0.22$).

along the midline of the attractive patch of the particle $(1,2,3),(2,3,4),(3,4,5),...,(48,49,50)$ (as shown in the right panel of Fig. 12), where the local curvature of is the radius of the circle defined by that triplet. For each curvamer, we compute a mean curvature radius, r_n, by averaging those radii along the length of the particle.

Appendix H: Escape of curvamer stacking assembly

The gap between the curvamers in two representative curvamer stack assemblies (shown in Fig. 4b of the main manuscript) is measured. We define this gap as δ' and show that the ratio of this gap to the maximum gap δ increases in the case of long-ranged interaction $\frac{\sigma}{\delta} = 0.65$ (Fig. 14).

The escape through long-ranged interaction was investigated using the energy per curvamer plots as shown below in Fig. 15. The largest stacks found in these plots – $N_{min} = 69$ for $\sigma/\delta = 0.22$, $N_{min} = 39$ for $\sigma/\delta = 0.43$, and $N_{min} = 25$ for $\sigma/\delta = 0.65$ correspond to the largest H values shown on the plots of Fig. 4a in the main manuscript.

Appendix I: Ground states vs. stack initialization

We have examined multiple initial stack configurations and found that the concentric stack with conformal contact is the configuration closest to the $T = 0$ ground state. As shown in Fig. 16 (b-c), we achieved the self-limiting stack with the lowest energy ($N_{min} = 8$) using

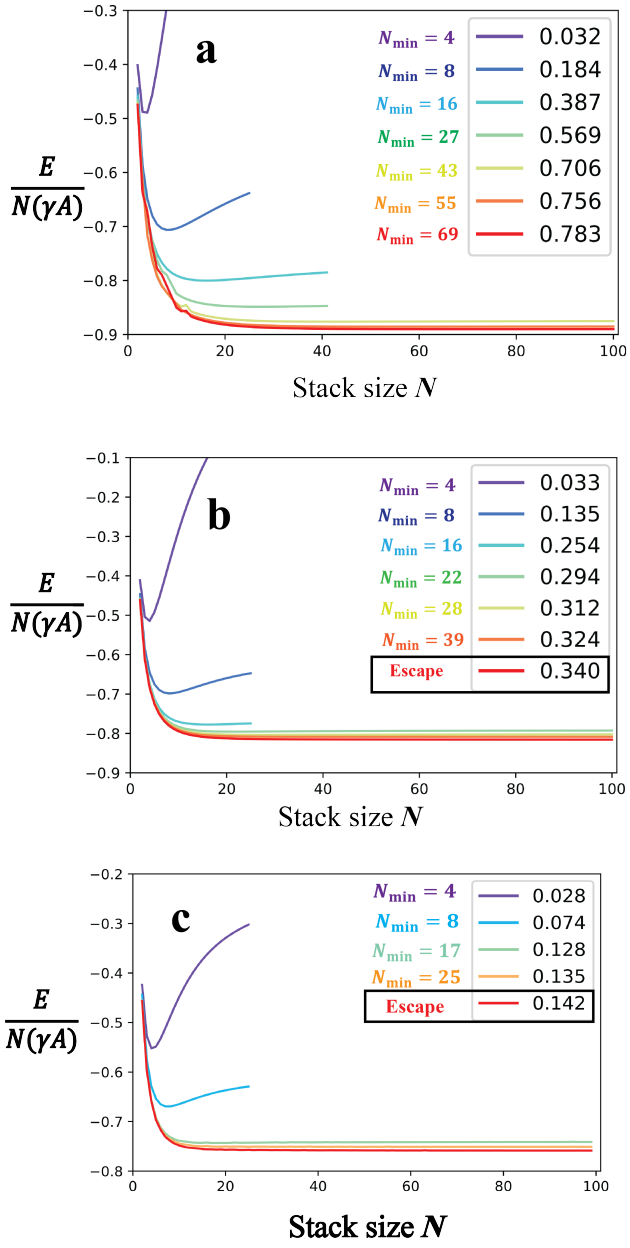

Figure 15. **(a)** Energy per curvamer plots as a function of stack size for different values of S ($\sigma/\delta = 0.22$). Because of the short-ranged interaction, stack size as large as $N_{min} = 69$ is observed for $S = 0.783$. **(b)** Energy per curvamer plots as a function of stack size for different values of S ($\sigma/\delta = 0.43$). No energy minimum was found while searching for stack size up to $N = 100$ for $S = 0.340$, resulting in an escape at a smaller value of S compared to the case of (a). The largest possible stack size in this case is $N_{min} = 39$. **(c)** Energy per curvamer plots as a function of stack size for different values of S ($\sigma/\delta = 0.65$). The largest stack found in this case is even smaller ($N_{min} = 25$) at $S = 0.142$.

this initial condition, for both conjugate gradient and simulated annealing algorithms. The other two initial conditions (one where all particles have radius r_0, another where every other particle has radius r_0, shown in Fig. 16a) result in the formation of two substacks with $N = 4$, which has higher energy compared to the $N = 8$ stack. A stack of flattened curvamers also find the energy minimum at $N_{min} = 8$. These observations point to the kinetic barrier related to the merging of two substacks of $N = 4$.

[1] B. Li, D. Zhou, and Y. Han, Assembly and phase transitions of colloidal crystals, Nature Reviews Materials **1** (2016).

[2] N. Vogel, M. Retsch, C.-A. Fustin, A. del Campo, and U. Jonas, Advances in colloidal assembly: The design of structure and hierarchy in two and three dimensions, Chemical Reviews **115**, 6265 (2015).

[3] F. Li, D. P. Josephson, and A. Stein, Colloidal assembly: The road from particles to colloidal molecules and crystals, Angewandte Chemie International Edition **50**, 360 (2011).

[4] W. Li, H. Palis, R. Mérindol, J. Majimel, S. Ravaine, and E. Duguet, Colloidal molecules and patchy particles: complementary concepts, synthesis and self-assembly, Chemical Society Reviews **49**, 1955 (2020).

[5] G. M. Grason, Perspective: Geometrically frustrated assemblies, The Journal of Chemical Physics **145**, 110901 (2016).

[6] G. Meng, J. Paulose, D. R. Nelson, and V. N. Manoharan, Elastic instability of a crystal growing on a curved surface, Science **343**, 634 (2014).

[7] D. M. Hall, I. R. Bruss, J. R. Barone, and G. M. Grason, Morphology selection via geometric frustration in chiral filament bundles, Nature Materials **15**, 727 (2016).

[8] M. Lenz and T. A. Witten, Geometrical frustration yields fibre formation in self-assembly, Nature Physics **13**, 1100 (2017).

[9] J. F. Berengut, C. K. Wong, J. C. Berengut, J. P. K. Doye, T. E. Ouldridge, and L. K. Lee, Self-limiting polymerization of dna origami subunits with strain accumulation, ACS Nano **14**, 17428 (2020).

[10] S. Meiri and E. Efrati, Cumulative geometric frustration in physical assemblies, Physical Review E **104**, 054601 (2021).

[11] B. Tyukodi, F. Mohajerani, D. M. Hall, G. M. Grason, and M. F. Hagan, Thermodynamic size control in curvature-frustrated tubules: Self-limitation with open boundaries, ACS Nano (in press) 10.1021/acsnano.2c00865 (2022).

[12] F. Serafin, J. Lu, N. Kotov, K. Sun, and X. Mao, Frustrated self-assembly of non-euclidean crystals of nanoparticles, Nature Communications **12**, 4925 (2021).

[13] M. Zhang, D. Grossman, D. Danino, and E. Sharon, Shape and fluctuations of frustrated self-assembled nano ribbons, Nature Communications **10**, 3565 (2019).

[14] Y. Yang, R. B. Meyer, and M. F. Hagan, Self-limited self-assembly of chiralnfilaments, Physical Review Letters **104**, 258102 (2010).

[15] T. S. Baker, N. H. Olson, and S. D. Fuller, Adding the third dimension to virus life cycles: Three-dimensional reconstruction of icosahedral viruses from cryo-electron micrographs, Microbiology and Molecular Biology Reviews **63**, 862 (1999).

[16] A. Zlotnick and S. Mukhopadhyay, Virus assembly, allostery and antivirals, Trends in Microbiology **19**, 14 (2011).

[17] R. Zandi, B. Dragnea, A. Travesset, and R. Podgornik, On virus growth and form, Physics Reports On virus growth and form, **847**, 1 (2020).

[18] C. A. Kerfeld, S. Heinhorst, and G. C. Cannon, Bacterial Microcompartments, Annual Review of Microbiology **64**, 391 (2010).

[19] C. Chowdhury, S. Sinha, S. Chun, T. O. Yeates, and T. A. Bobik, Diverse bacterial microcompartment organelles, Microbiology and Molecular Biology Reviews : MMBR **78**, 438 (2014).

[20] R. O. Prum, E. R. Dufresne, T. Quinn, and K. Waters, Development of colour-producing β-keratin nanostructures in avian feather barbs, Journal of The Royal Society Interface **6**, S253 (2009).

[21] E. R. Dufresne, H. Noh, V. Saranathan, S. G. J. Mochrie, H. Cao, and R. O. Prum, Self-assembly of amorphous biophotonic nanostructures by phase separation, Soft Matter **5**, 1792 (2009).

[22] V. Saranathan, J. D. Forster, H. Noh, S.-F. Liew, S. G. J. Mochrie, H. Cao, E. R. Dufresne, and R. O. Prum, Structure and optical function of amorphous photonic nanostructures from avian feather barbs: a comparative small angle x-ray scattering (saxs) analysis of 230 bird species, Journal of The Royal Society Interface **9**, 2563 (2012).

[23] J. W. Weisel, Structure of fibrin: impact on clot stability, Journal of Thrombosis and Haemostasis **5**, 116 (2007).

[24] D. Popp and R. C. Robinson, Supramolecular cellular filament systems: How and why do they form?, Cytoskeleton **69**, 71 (2012).

[25] M. F. Hagan and G. M. Grason, Equilibrium mechanisms of self-limiting assembly, Reviews of Modern Physics **93**, 025008 (2021).

[26] F. Osawa and S. Asakura, *Thermodynamics of the polymerization of protein* (Academic Press, London; New York, 1975).

[27] J. N. Israelachvili, *Intermolecular and Surface Forces* (Elsevier, 2011).

[28] S. Schneider and G. Gompper, Shapes of crystalline domains on spherical fluid vesicles, Europhysics Letters (EPL) **70**, 136 (2005).

[29] R. Ghafouri and R. Bruinsma, Helicoid to spiral ribbon transition, Physical Review Letters **94**, 138101 (2005).

[30] S. Armon, H. Aharoni, M. Moshe, and E. Sharon, Shape selection in chiral ribbons: from seed pods to supramolecular assemblies, Soft Matter **10**, 2733 (2014).

[31] G. M. Grason, Chiral and achiral mechanisms of self-limiting assembly of twisted bundles, Soft Matter **16**, 1102 (2020).

[32] J. P. Sethna and M. Kléman, Spheric domains in smectic liquid crystals, Physical Review A **26**, 3037 (1982).

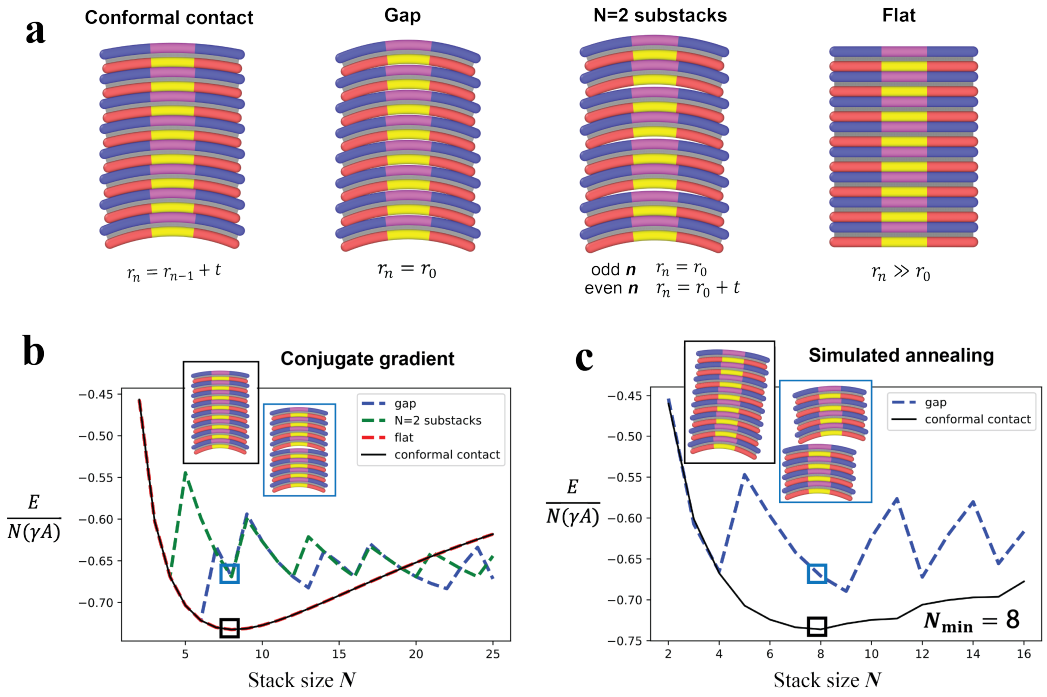

Figure 16. **(a)** Different initial geometry of a curvamer stack of $N = 8$: curvature-focused stack with conformal contact ($r_n = r_{n-1} + t$), gapped stack ($r_n = r_0$), an ensemble of $N = 2$ substacks, and stack of flattened curvamers ($r_n >> r_0$).**(b)** Energy per curvamer plot calculated using the conjugate gradient algorithm for four different initial conditions presented in (a). **(c)** Energy per curvamer plot calculated using simulated annealing for initial conditions of curvature-focused state and gapped state. Using both energy minimization algorithms (b-c), the energy minimum at $N_{min} = 8$ is found when initial conditions of curvature-focused and flattened curvamer stack were applied.

[33] J.-b. Fournier and E. G. Virga, Geometrical exact solutions for confocal lamellar textures yielding confinement and faceting phenomena, Proceedings of the Royal Society of London. Series A: Mathematical, Physical and Engineering Sciences **452**, 1251 (1996).

[34] B. A. DiDonna and R. D. Kamien, Smectic blue phases: Layered systems with high intrinsic curvature, Physical Review E **68**, 041703 (2003).

[35] J. Nye and F. J. Wright, Natural focusing and fine structure of light: Caustics and wave dislocations, American Journal of Physics **68**, 776 (2000).

[36] C. Fernández-Rico, M. Chiappini, T. Yanagishima, H. de Sousa, D. G. A. L. Aarts, M. Dijkstra, and R. P. A. Dullens, Shaping colloidal bananas to reveal biaxial, splay-bend nematic, and smectic phases, Science **369**, 950 (2020), https://www.science.org/doi/pdf/10.1126/science.abb4536.

[37] M. Chaippini and M. Dijkstra, A generalized density-modulated twist-splay-bend phase of banana-shaped particles, Nature Communications **12**, 2157 (2021).

[38] I. Niv and E. Efrati, Geometric frustration and compatibility conditions for two-dimensional director fields, Soft Matter **14**, 424 (2018).

[39] S. Meiri and E. Efrati, Cumulative geometric frustration and superextensive energy scaling in a nonlinear classical xy-spin model, Phys. Rev. E **105**, 024703 (2022).

[40] Well above the onset of aggregation (i.e. in supersaturated conditions) the (ideal) per subunit translation entropy in large aggregates is generically a negligible fraction of the free energy [25, 50] , and the properties of *finite size* aggregation derive almost entirely from minima of intra-assembly free energy per subunit, a quantity the derives from the size dependence physical interactions within the aggregate (i.e. adhesion and elasticity) and as well as entropy of fluctuations *within* the aggregate.

[41] A. P. Thompson, H. M. Aktulga, R. Berger, D. S. Bolintineanu, W. M. Brown, P. S. Crozier, P. J. in 't Veld, A. Kohlmeyer, S. G. Moore, T. D. Nguyen, R. Shan, M. J. Stevens, J. Tranchida, C. Trott, and S. J. Plimpton, Lammps - a flexible simulation tool for particle-based materials modeling at the atomic, meso, and continuum scales, Computer Physics Communications **271**, 108171 (2022).

[42] $N_{\min}$ corresponds to the dominant aggregate size in the canonical ensemble, well above the critical aggregation concentration [25].

[43] T. van Manen, S. Janbaz, and A. A. Zadpoor, Programming the shape-shifting of flat soft matter, Materials Today **21**, 144 (2018).

[44] C. Sigl, E. M. Willner, W. Engelen, J. A. Kretzmann, K. Sachenbacher, A. Liedl, F. Kolbe, F. Wilsch, S. A. Aghvami, U. Protzer, M. F. Hagan, S. Fraden, and H. Dietz, Programmable icosahedral shell system for virus trapping, Nature Materials **20**, 1281 (2021).

[45] D. Hayakawa, T. E. Videbaek, D. M. Hall, H. Fang, C. Sigl, E. Feigl, H. Dietz, S. Fraden, M. F. Hagan, G. M. Grason, and W. B. Rogers, Geometrically programmed self-limited assembly of tubules using dna origami colloids, arXiv:2203.01421 [cond-mat] (2022).

[46] E. Epstein, J. Yoon, A. Madhukar, K. J. Hsia, and P. V. Braun, Colloidal particles that rapidlychange shape via elastic instabilities, Small **11**, 6051 (2015).
[47] T. G. Mason, Osmotically driven shape-dependent colloidal separations, Physical Review E **66**, 060402 (2002).
[48] W. B. Rogers and J. C. Crocker, Direct measurements of dna-mediated colloidal interactions and their quantitative modeling, Proceedings of the National Academy of Sciences **108**, 15687 (2011), publisher: Proceedings of the National Academy of Sciences.
[49] J. Bae, T. Ouchi, and R. C. Hayward, Measuring the elastic modulus of thin polymer sheets by elastocapillary bending, ACS Applied Materials & Interfaces **7**, 14734 (2015).
[50] J. Groenewold and W. K. Kegel, Anomalously large equilibrium clusters of colloids, The Journal of Physical Chemistry B **105**, 10.1021/jp011646w (2001).